Research Article

The effect of defects formed under pressure on $CuCrO_2$ delafossite

C. Boyraz[1] · P. Aksu[2] · A. Guler[3] · L. Arda[4]

Received: 4 January 2022 / Accepted: 25 May 2022
Published online: 06 June 2022

Abstract
Pressure-dependent delafossite $CuCrO_2$ samples are synthesized by the solid-state reaction method to investigate the effect of defects formed under pressure on the structure and magnetic properties of $CuCrO_2$. X-ray Diffractometer, Scanning Electron Microscope (SEM), Energy Dispersive Spectroscopy (EDS), Photoluminescence spectroscopy (PL), and Vibrating Sample Magnetometer (VSM) are used the characterize $CuCrO_2$ samples. All samples give almost the same structural phase properties without any secondary peaks. All magnifications of SEM images show no melting of the sample and thus the annealing temperature of the samples is optimized. Photoluminescence measurements reveal that near band emission is caused by excitonic transitions between electrons and holes, the stronger the UV emission of the sample, the higher the crystallization quality, and fewer defects occur. Magnetic investigations depict that the spins are antiferromagnetically oriented while they have a magnetic moment component perpendicular to the plane. Therefore, each grain should be considered a weak magnet. Temperature-dependent magnetic moment measurements exhibit a slight variation in moment values. The reason behind this should be attributed to the grain size related to the formation of grains by applied pressure.

Article Highlights

1. The solid-state reaction method is used to synthesize pressure-dependent delafossite $CuCrO_2$ samples.
2. The solid-state reaction process and pressure effect may cause cooper and oxygen vacancies of the $CuCrO_2$ samples.
3. In all samples below 100 K, there might be antiferromagnetic behavior and above 100 K paramagnetic behavior actively occur.

Keywords Delafossite $CuCrO_2$ · Structural and magnetic properties · Optical transmittance · Photoluminescence properties

✉ L. Arda, lutfi.arda@eng.bau.edu.tr | [1]Faculty of Technology, Department of Mechanical Engineering, Marmara University, Maltepe, 34840 Istanbul, Turkey. [2]Institute of Nanotechnology, Gebze Technical University, Gebze, 41400 Kocaeli, Turkey. [3]Faculty of Technology, Department of Electrical and Electronics Engineering, Marmara University, Maltepe, 34840 Istanbul, Turkey. [4]Faculty of Engineering and Naturel Sciences, Department of Mechatronic Engineering, Bahcesehir University, Ciragan Cad. Osmanpasa Mektebi Sok, Besiktas, 34349 Istanbul, Turkey.

1 Introduction

Developing metal oxide-based transparent electronics in the rapidly expanding semiconductor industry is one of the priority research areas. In industrial applications, discovering the controllability of physical properties for materials is an essential fact and desired factor. A controllable multiferroic has been found with inherent geometric magnetic frustration [1–4]. $CuCrO_2$ (delafossite oxide) is in the group of systems having an antiferromagnetic triangular sublattice and this trivalent cationed system possesses the space group of $R\bar{3}m$ in the hexagonal setting. Due to the discovery of its multiferroic behavior, the magnetic behaviors of defalossite $CuCrO_2$ receive detailed interest [5–7]. Further, $CuCrO_2$ exhibits interesting magnetoelectric properties which are tunable by both a magnetic and an electric field [7–9]. In the optoelectronic device technology, n-type transparent conducting oxides (TCOs), such as Sn-doped In_2O_3 [10], Sb-doped SnO_2 [11], and Al-doped ZnO [12] are some of the well-known and widely-used examples in touch panels, solar cells, and flat panels. However, the p-type of TCOs are relatively less developed and therefore less widely utilized. By achieving the first $CuAlO_2$ film, a new highly conductive p-type TCO candidate has been found and this conducted research brought new Cu-incorporation oxides trials like $CuFeO_2$ [13] and $CuInO_2$ [14]. Intrinsically, the low hole mobility of p-type TCOs gives rise to low conductivity, and therefore the research, together with development efforts for p-type TCOs is still a worthwhile issue. So far, many methods have been carried out to synthesize n-type semiconductor nanoparticles through different methods such as titanium dioxide (TiO_2) [15], zinc oxide (ZnO) [16], and tin dioxide (SnO_2) [17] but the number of reports on p-type transparent oxide semiconductor (TOS) nanoparticles needs to be increased by conducting research and discoveries. As a p-type TCO, $CuCrO_2$ is an interesting material of which elemental components are non-toxic, inexpensive, and considerable for industrial purposes. At room temperature, $CuCrO_2$ has the property of varying a direct optical band gap as large as 2.95–3.30 eV in bulk shape, and this varying bandgap property of $CuCrO_2$ is crucial in bandgap engineering [18–20].

In this presented study, the pressure effect on the physical properties of $CuCrO_2$ is investigated. The samples are subjected to 10, 30, and 50 tons of pressure and coded as S1, S2, and S3, respectively. The technical measurement properties such as structure, optic, and magnetic properties are detailed in the experimental section. The results and discussion section exhibits and discusses the obtained results and correlates them with the literature. Finally, the conclusion section provides an overview of the conducted research with some important details.

2 Experimental

Cu_2O and Cr_2O_3 chemicals provided by Sigma-Aldrich were subjected to thorough mixing of Redox reaction ($Cu_2O + Cr_2O_3 2CuCrO_2$). The mixture was sintered in a furnace by increasing the final temperature to 900 °C for 2.5 h. The furnace then was switched-off for self-cooling to room temperature. The samples were taken out and ground by an agate mortar and pressed for 10, 30, and 50 MPa pressures for 10 min with a thickness of 4 mm and a diameter of 10 mm. For better atomic packing, a second time sintering was applied for all samples by increasing the temperature by 4 °C/min. The sample was kept at the final temperature of 1100 °C for 3 h and taken out the samples after self-cooling to room temperature. The crystallinity of the synthesized powder was analyzed by Rigaku Automated Multipurpose X-ray Diffractometer (XRD) instrument using a monochromated Cu Kα (1.5418 Å) source in the 2θ scan range of 10° to 120°. The defined surface morphology and sample stoichiometry was provided by Jeol-6390-LV Scanning Electron Microscopy (SEM–EDX) tool. A special design X-ray Photoelectron Spectroscopy tool was used to measure the core levels of all species at the surface of the samples. The optical properties of the samples were clarified by Shimadzu 2600 UV-Spectrophotometer in the range of 200–900 nm. Photoluminescence properties were measured by using the Agilent Cary Eclipse Fluorescence Spectrophotometer. Quantum Design Model 6000Vibrating Sample Magnetometer (VSM) for Physical Property Measurement System (PPMS) was used to measure magnetic parameters.

3 Result and discussions

3.1 Structural study

A detailed X-ray study was provided for the samples S1, S2, and S3 in a wide range of 10–110°. As seen in Fig. 1, all samples give almost the same structural phase properties without any secondary peaks. $CuCrO_2$ system has the trigonal crystal structure with the space group of $R\bar{3}m$. The lattice parameters were calculated by Cohen's method for S1, S2, and S3 samples as (a = 2.976°A and c = 17.110°A), (a = 2.972°A and c = 17.107°A), and (a = 2.969°A and c = 17.109°A), respectively [21]. The results were also proofed by NIMS database. The effect of pressure on lattice parameters and unit cell volume was demonstrated in

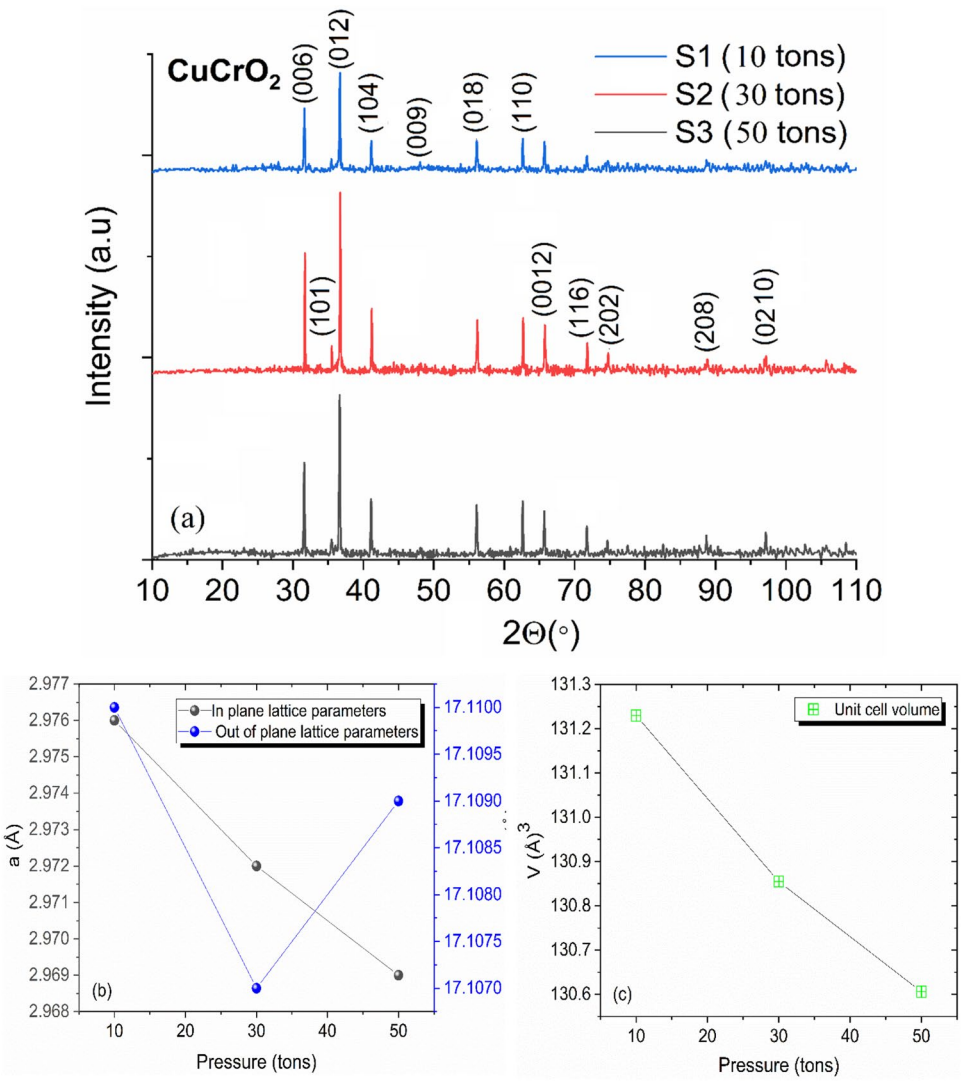

Fig. 1 XRD patterns of pressure-dependent $CuCrO_2$ samples in (**a**). The variation of pressure-dependent in-plane and out-of-plane lattice parameters and the unit cell variation with pressure was demonstrated

Fig. 1b and c respectively. The in-plane lattice parameters are in decrement tendency with increasing applied pressure but out of plane lattice parameters show a decrease up to 30 tons of pressure and an increase after 30 tons. The unit cell volume is in the decrement tendency with applied pressure, so this is an indication of increasing chemical pressure in the cell volume.

Figure 2 depicts the SEM macro images in 5 µm, 1 µm, and 500 nm magnifications to figure out the granular behavior of the S1, S2, and S3 samples. As seen in all magnifications of SEM images, no melting was found and thus the annealing temperature of the samples was optimized.

3.2 Photoluminescence (PL)

PL measurements of the $CuCrO_2$ sample were induced in the range of 350 nm to 900 nm as shown in Fig. 3. Two main peaks were observed in Fig. 3 which are ultraviolet (UV) emission peak and broad visible emission band (DL). In the UV region, a sharp transition peak, attribute to near band edge (NBE) transitions, was observed at 362 and 378 nm for the $CuCrO_2$ sample. NBE emission is caused by excitonic transitions between electrons and holes, the stronger the UV emission of the sample, the higher the crystallization quality, and fewer defects occurred. The second dominant and broad emission peak is Deep-level (DL) emission, consisting of violet, blue-green-yellow-orange, and red emission peaks. Deep-level emission is adjusted impurities or defects such as Cu-interstitial (Cui), Cu vacancies (V_{cu}), Cr vacancy (V_{cr}), oxygen vacancies (Vo), and oxygen interstitial (O_i) in the crystal structure. Therefore, the Gaussian decomposition of PL spectra was analyzed by "Fityk" software. To our knowledge, such PL emission has not been reported for $CuCrO_2$ delafossit oxides in the literature.

The eight Gaussian decompositions of PL spectra versus emission wavelength were plotted as shown in Fig. 4. The peak labels with positions center, areas, and height of

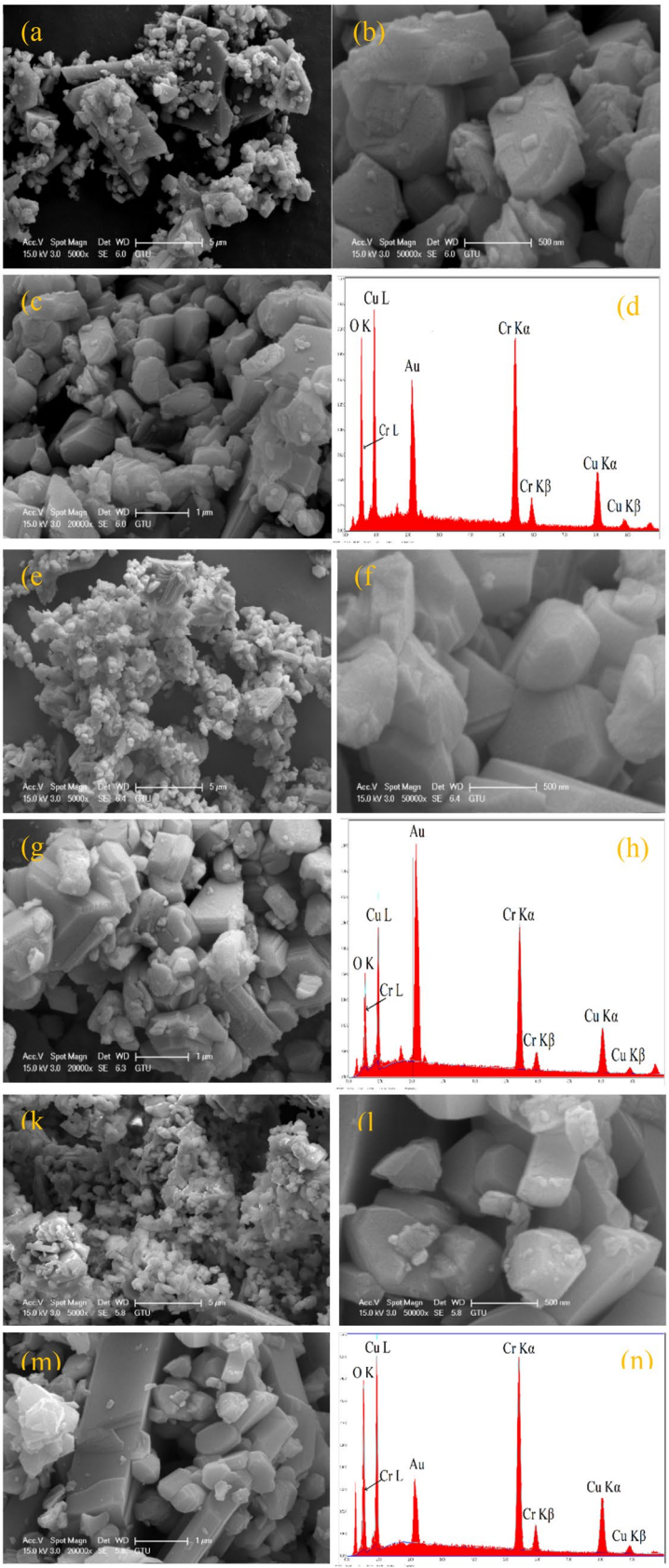

Fig. 2 SEM images at varying magnifications and EDX spectrums of S1, S2, and S3 samples. In the figure **a**, **b**, **c**, and **d** are belong to S1, **e**, **f**, **g**, and **h** are belong to S2, and **k**, **l**, **m**, and **n** are belong to S3 samples

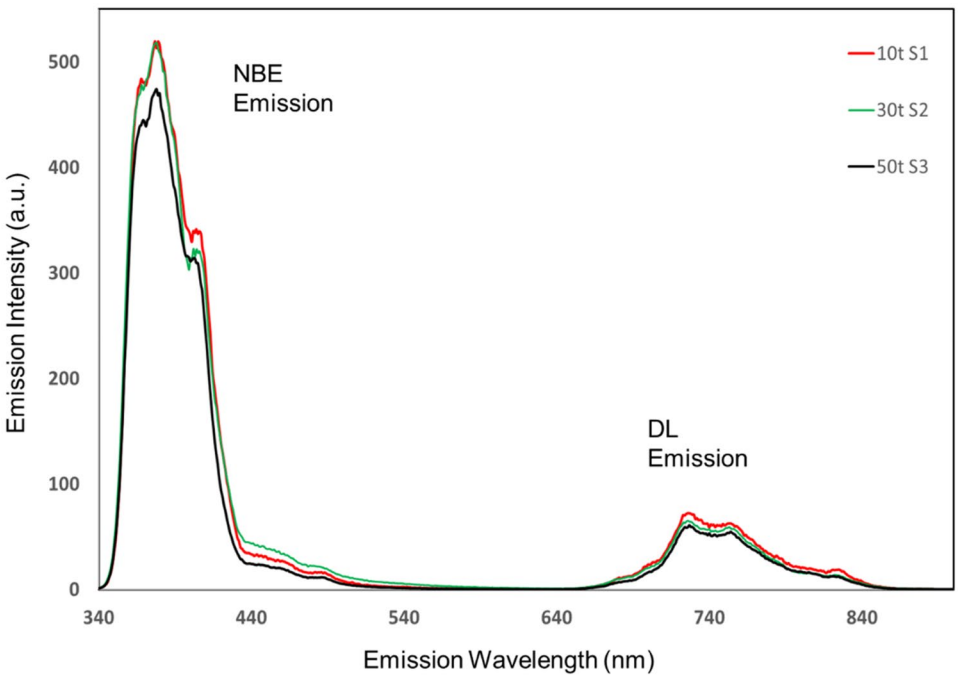

Fig. 3 PL spectra of the $CuCrO_2$ sample

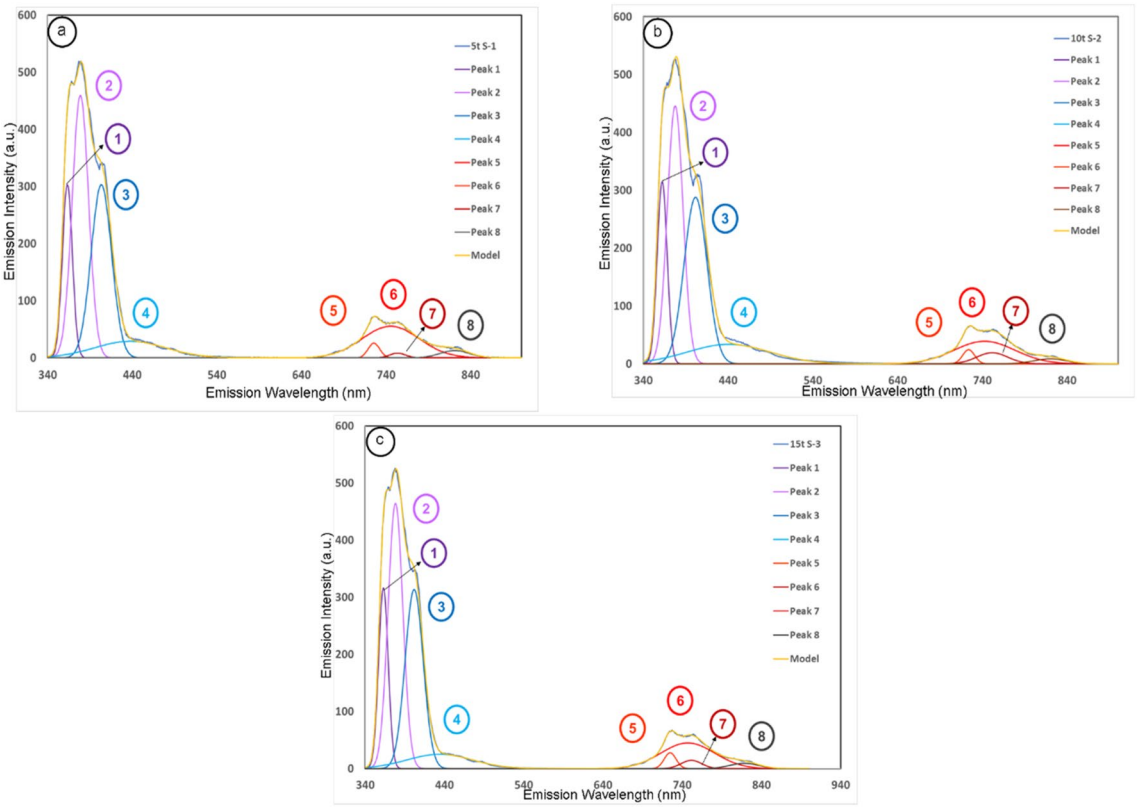

Fig. 4 Gaussian decomposition of PL spectra of $CuCrO_2$ samples at various pressures **a** 10t, **b** 30t, and **c** 50t

these curves varied according to the various pressure of $CuCrO_2$ samples as indicated in Table 1. The eight peaks are suited to five emissions; two ultraviolet emissions (Peak 1 and Peak 2) from 360 to 390 nm can be ascribed to the NBE of $CuCrO_2$ as an indication of the excitonic characteristic. Violet and blue emissions (Peak 3 and Peak 4) from

Table 1 The peak center, height, and area, values, emission range, the origin of PL emission of the $CuCrO_2$ samples

Peak Label	10t S1			30t S2			50t S3					
	Center	Height	Area	Center	Height	Area	Center	Height	Area	Emission range	Origin	
Peak 1	363	304	4452.3	362	315	4601.2	363	316	4744	Ultraviolet	Excitons	NBE emission
Peak 2	379	460	11,138	378	446	10,345	378	465	10,849	Ultraviolet	Excitons	
Peak 3	403	303	9198.9	402	288	9731.9	402	314	8957	Violet	Cu-interstitial	DL emission
Peak 4	437	29	3057.4	441	34	4112.8	434	25	2622	Blue	Vcu	
Peak 5	726	26	439	743	39	3526.3	725	28	519.2	Red	Vo	
Peak 6	745	55	4682.4	724	24	426	752	14	459	Red	Vo	
Peak 7	754	8	192	752	20	896	747	45	3,811	NIR (near-infrared)	Vo	
Peak 8	821	13	553	820	9	437	818	9	419	NIR (near-infrared)	Vo	

390 to 492 nm can be attributed to Cu-interstitial and Cu vacancies, respectively, and the red emission is divided into two parts; (Peak 5 and Peak 6) from 620 to 750 nm and (690–750 nm) might be attributed to oxygen interstitials (O_i) and oxygen vacancy (V_o), respectively. Two NIR (near-infrared) emissions (Peak 7 and Peak 8) from 750 to 768 nm were the results of oxygen vacancy depicted [22] and references in]. Moreover, it can be attributed to the second-order diffraction (a harmonic of the first peak of the near band-edge) [20].

As seen in Fig. 4, the DL emission (visible region) band consists of violet, red, and NIR emission peaks for the $CuCrO_2$ samples. It can be concluded that reactions in the solid-state reaction process may cause cooper and oxygen vacancies and affect the luminescence, and structural and magnetic properties of the $CuCrO_2$ sample.

3.2.1 Band gap calculation

The values of E_g depended on several factors such as crystallite size, carrier concentration, lattice strain, and the size effect of the dopant metals in the $CuCrO_2$ lattice. The optical band gap E_g can be found using the following equation for the absorption coefficient (α) and the photon energy (hv):

$$\alpha h\upsilon = k\left(h\upsilon - E_g\right)^{1/n} \tag{1}$$

In Eq. (1), E_g and k is the optical band gap and energy-independent constants, respectively. Since $F(R_\alpha)$ is proportional to α and n is a constant that depends on the bandgap type 1/2 and 2 for direct and indirect bandgaps, respectively. Thus, for directly and indirectly allowed transitions, n is taken as 1/2 and 2 Eq. (1) can be transformed to Eq. (2):

$$F\left(R_\alpha\right)h\upsilon = k\left(h\upsilon - E_g\right)^{1/2} \quad \text{and} \quad F\left(R_\alpha\right)h\upsilon = k\left(h\upsilon - E_g\right)^{2} \tag{2}$$

in other words, $(F(R_\alpha)h\upsilon)^2 = k^2(h\upsilon - E_g)$. and $(F(R_\alpha)h\upsilon)^{1/2} = k^{1/2}(h\upsilon - E_g)$.

The slope of the graph of $\left(F\left(R_\alpha\right)h\upsilon\right)^2$ was approximated by using a linear fit $y(h\upsilon) = A \times h\upsilon + B$ in the least-squares sense [23]. To do this, the following error formula given in Eq. (3)

$$E(A,B) = \min_{A,B} \sum_{i=1}^{N} \left[A \times (h\upsilon)_i + B - \left(\left(F\left(R_\alpha\right)h\upsilon\right)^2\right)_i\right]^2 \tag{3}$$

was minimized for A and B where N is the number of data points. Tables 2 and 3 displays A, B, Eg-direct and indirect band gap energies and relative error values for these data set.

As shown in Tables 2 and 3 and Fig. 5, the direct and indirect bandgap energy (E_g-direct and E_g-indirect) were calculated by the linear approximation of the graphical slope of $(F(R_\alpha)hu)^2$ and $(F(R_\alpha)hu)^{0.5}$ to the photon energy axis in which, $F(R_\alpha) = 0$. In other words, the E_g value was obtained from the intersection between the linear fit and the photon energy axis. As shown in Fig. 5, the direct-I and direct-II bandgap energies of the $CuCrO_2$ samples were observed as (1.86, 1.87, and 1.90 eV) and (2.41, 2.41, and 2.47 eV) respectively. The indirect-I and indirect-II bandgap energies of the $CuCrO_2$ samples were observed as (1.50, 1.51, and 1.58 eV) and (1.65, 1.66, and

Table 2 Fitting the curve function y(hu) = A × hu + B, Eg-direct (eV) bandgap energies and relative errors for $CuCrO_2$ samples

Sample code	I				II			
	A	B	Eg-direct (eV)	Rel. Error	A	B	Eg-direct (eV)	Rel. Error
S1	1.5512	−2.9076	1.87	0.00669	2.0891	−5.0387	2.41	0.00350
S2	0.3309	−0.6212	1.88	0.00688	0.4469	−1.0791	2.41	0.00615
S3	0.7206	−1.3701	1.90	0.00428	1.0980	−2.7157	2.47	0.00475

Table 3 Fitting the curve function y(hu) = A × hu + B, E_g-indirect (eV) bandgap energies and relative errors for $CuCrO_2$ samples

	I				II			
Sample code	A	B	Eg-indirect (eV)	Rel. Error	A	B	Eg-indirect (eV)	Rel. Error
S1	1.3075	− 1.9579	1.50	0.00202	0.8492	− 1.4093	1.66	0.00011
S2	0.9138	− 1.3830	1.51	0.00244	0.5607	− 0.9157	1.63	0.00025
S3	1.2150	− 1.9214	1.58	0.00382	0.7945	− 1.4423	1.82	0.00011

1.82 eV), respectively. It was found that the direct and indirect bandgap of $CuCrO_2$ samples increased with the pressure. The values of Eg depended on the crystallite size, carrier concentration, lattice strain, the size effect of the dopant, and the effect of defects formed under pressure on $CuCrO_2$ delafossite.

3.3 Magnetic properties

We further investigated field-dependent magnetization for the samples S1, S2, and S3 under varying fixed temperatures (10, 50, 100, 180, 220, 300, and 400 K) separately. As seen in Fig. 6 except for the measurements at 10 and 50 K, all samples above 100 K show paramagnetic behavior. Below 100 K there might be antiferromagnetic behavior.

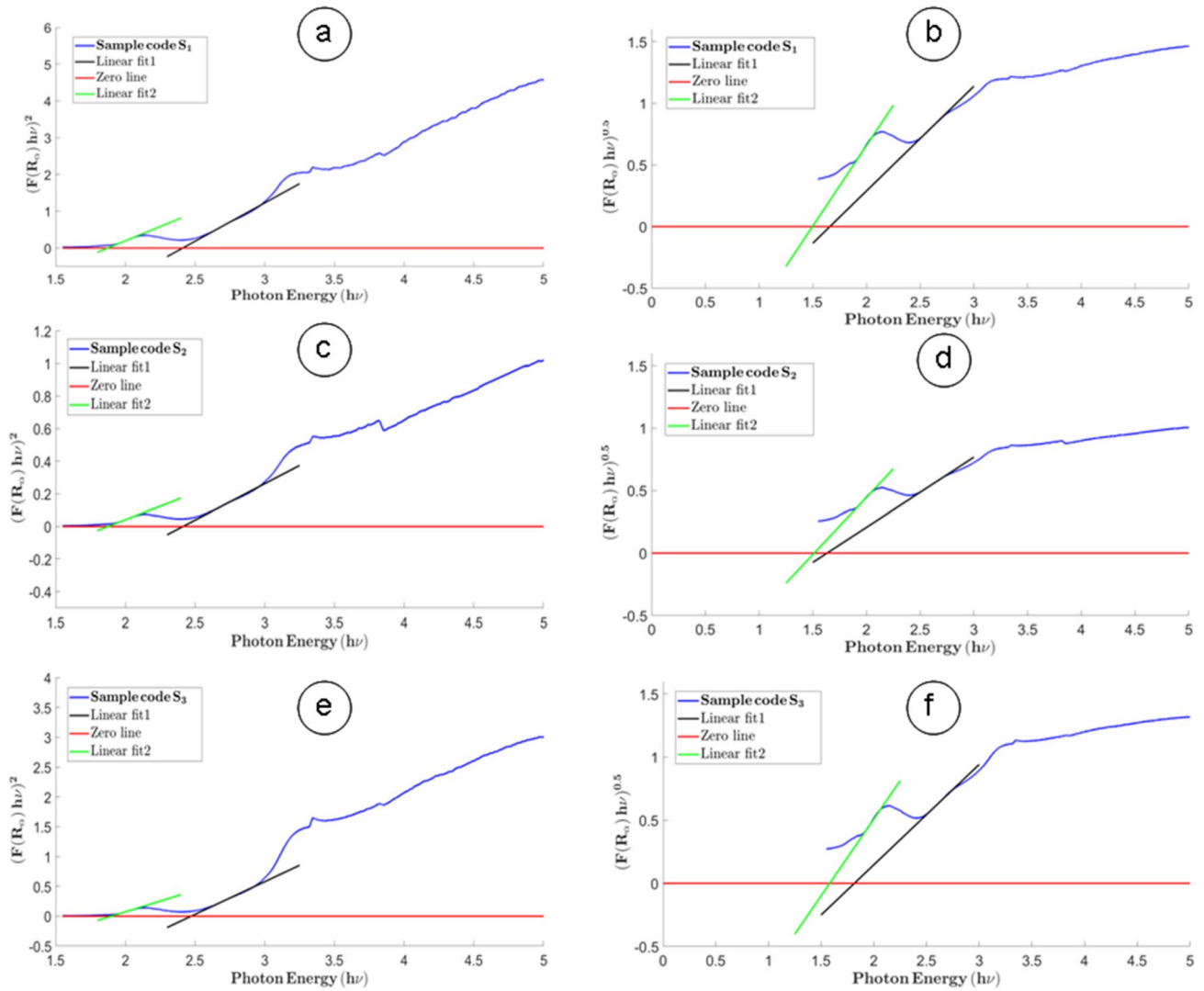

Fig. 5 The plots of **a**, **c**, and **e** exhibit photon energy-dependent $(F(R_\alpha)hv)^2$ behavior, and **b**, **d**, and **f** for $(F(R_\alpha)hv)^{0.5}$

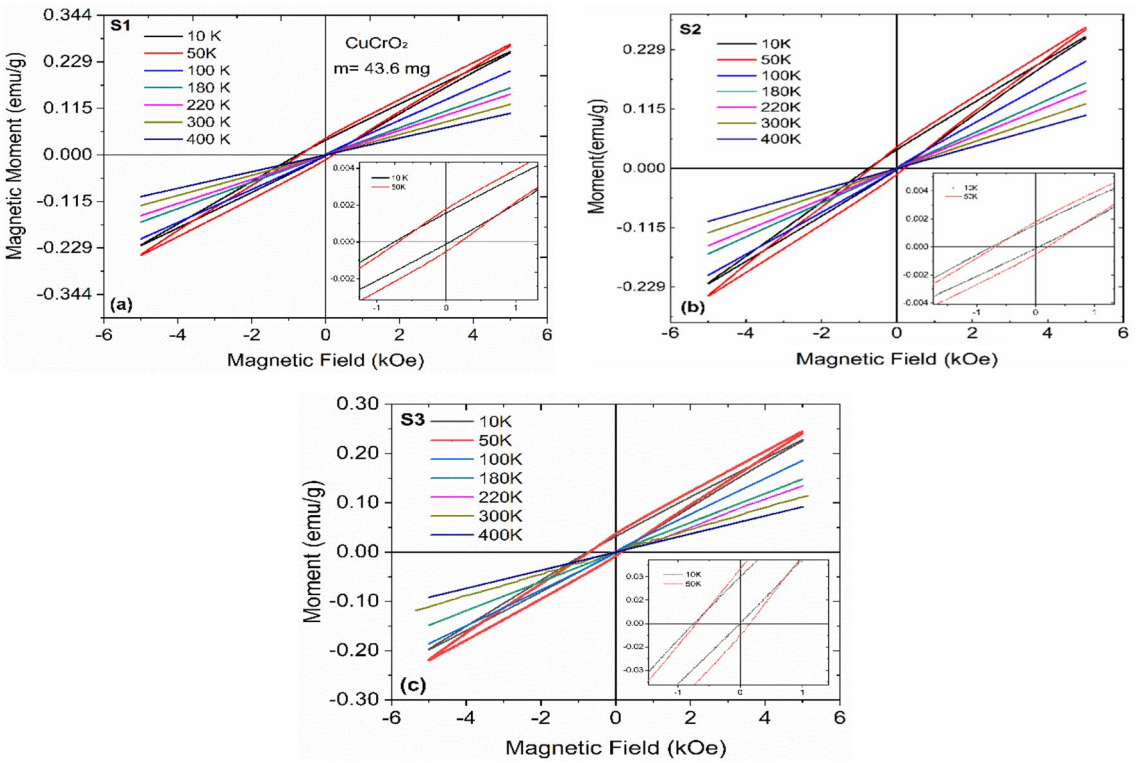

Fig. 6 Field-dependent moment variation in the magnetic field region ± 6 kOe

Table 4 Magnetic variations of S1, S2, and S3 samples at 10 and 50 K

Sample code	Remanent magnetisation M_r(emu/g)		Coercivity field H_c(Oe)	
	at 10 K	at 50 K	at 10 K	at 50 K
S1	$1.56*10^{-3}$	$1.79*10^{-3}$	−763	−498
S2	$1.60*10^{-3}$	$1.81*10^{-3}$	−727	−549
S3	$1.62*10^{-3}$	$1.14*10^{-3}$	−679	−492

Magnetic variations (Remanent Magnetisation and Coercivity Field) of S1, S2, and S3 samples at 10 and 50 K are shown in Table 4. In the delafossite structure, each linearly coordinated Cu by two oxygen atoms, forming O–Cu–O structures parallel to the c-axis. This is the form of a layered triangular lattice anti-ferromagnetic and oxygens in the O–Cu–O structure are each coordinated with three Cr atoms parallel to the ab plane.

However, due to the granular structure of the samples, magnetic behavior slightly to superparamagnetic behavior. This should be the reason for the pressure effect of each sample. The pressure effect much clearly seen in Fig. 7 which depicts the temperature-dependent moment behaviors of S1, S2, and S3 $CuCrO_2$ samples. As seen in Fig. 7, below 100 K, inter-grain magnetization gets in antiferromagnetic order. Each grain has a net magnetic moment, such that in a plane, the spins are antiferromagnetically oriented while they have a magnetic moment component perpendicular to the plane. Therefore, each grain should be considered a weak magnet. After 100 K in Fig. 7, all 3 samples showed the same decrement behavior. Before 100 K all samples exhibited a slight variation in moment values. The reason behind this should be attributed to the grain size, related to the formation of grains by applied pressure. The observed exchange bias in Fig. 6 (M-H measurements) reveals interfaces of grains that are not identical but active in the formation of coercive fields.

4 Conclusion

Pressure-dependent delafossite $CuCrO_2$ samples were synthesized by the solid-state reaction method. The effect of pressure was detailed in all samples revealing that almost all samples were at the same structural phase properties without any secondary peaks. Excitonic transitions between electrons and holes were revealed by near band emission of Photoluminescence measurements and using the stronger the UV emission of the sample, the higher the crystallization quality and fewer defects occurred. In PL measurements, the second

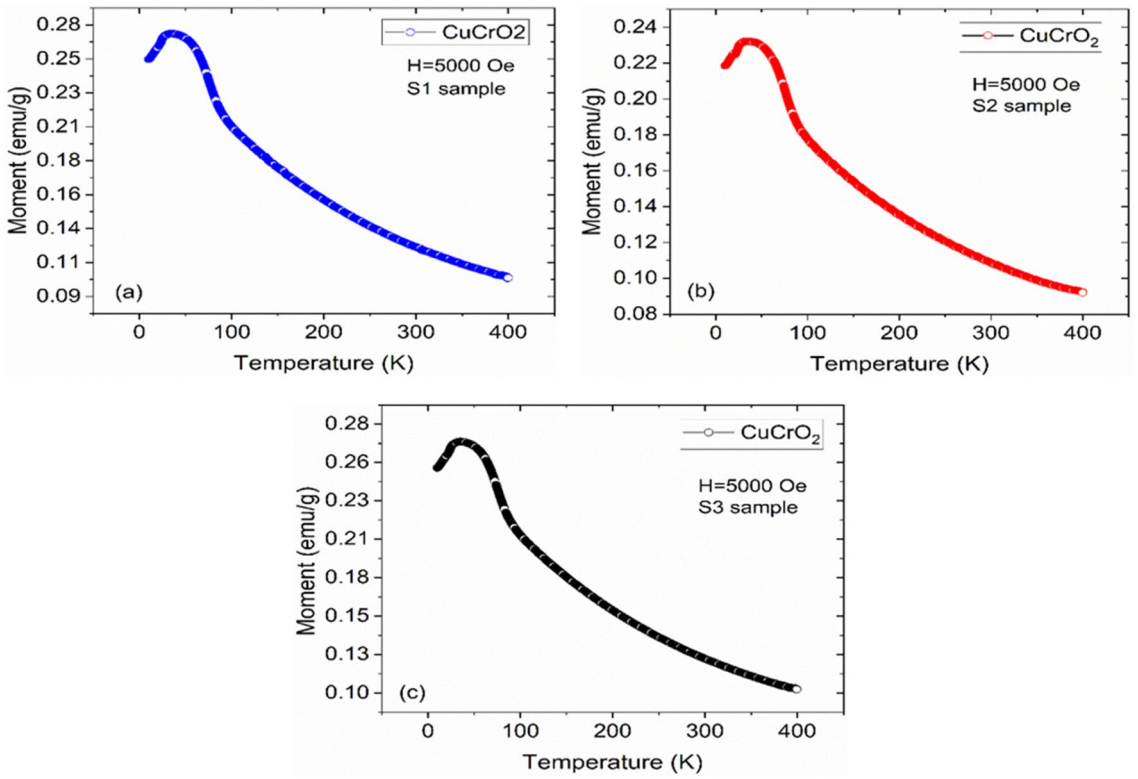

Fig. 7 Temperature-dependent moment variations of S1, S2, and S3 $CuCrO_2$ samples

dominant and broad emission peak was Deep-level (DL) emission adjusted impurities or defects such as Cu vacancies (V_{cu}), and oxygen vacancies (V_o), in the crystal structure. Below 100 K, inter-grain magnetization gets in antiferromagnetic order and at that temperature range, all samples exhibit a slight variation in moment values in Fig. 7. Magnetic field–dependent moment variations in Fig. 6 also supported the results of PL measurements due to the observed exchange bias shifts. The reason behind this should be attributed to the grain size related to the formation of grains by applied pressure, the vacancies revealed by PL measurements, and the sample synthesizing type affecting especially the physical properties.

Acknowledgements The presented work was supported by the Research Fund of Bahcesehir University (Project No: BAP-2021.01.27 and BAP.2019-01.04), Istanbul, Turkey

Author contributions CB Conceptualization, Methodology, Formal analysis and investigation, Validation, Writing-Reviewing and Editing, Writing- Original draft preparation, Writing- Reviewing and Editing. PA Methodology, Conceptualization, Methodology, Formal analysis and investigation, Validation, Writing- Original draft preparation. AG Conceptualization, Methodology, Formal analysis and investigation, Validation, Writing- Original draft preparation. LA Conceptualization, Methodology, Formal analysis and investigation, Validation, Writing-Reviewing and Editing, Writing- Original draft preparation, Validation, Writing- Reviewing and Editing, Supervision, and Funding acquisition.

Funding The presented work was supported by the Research Fund of Bahcesehir University (Project No: BAP-2021.01.27 and BAP.2019–01.04), Istanbul, Turkey

Data availability All data generated or analyzed during this study are included in this published article.

Declarations

Conflict of interest The authors declare that they have no known competing financial interests or personal relationships that could have appeared to influence the work reported in this paper.

Ethical approval This article does not contain any studies with human participants or animals performed by any of the authors.

References

1. Cheong SW, Mostovoy M (2007) Multiferroics: a magnetic twist for ferroelectricity. Nat Mater 6:13–20. https://doi.org/10.1038/nmat1804
2. Shannon RD, Rogers DB, Prewitt CT (1971) Chemistry of noble metal oxides. I. Syntheses and properties of ABO_2 delafossite compounds. Inorg Chem 10:713–718. https://doi.org/10.1021/IC50098A011
3. Barnabé A, Sabatier P, Mugnier E, Presmanes L, Tailhades P (2006) Preparation of delafossite $CuFeO_2$ thin films by rf-sputtering on conventional glass substrate. Mater Lett 60:3468–3470. https://doi.org/10.1016/j.matlet.2006.03.033
4. Matukhin VL, Khabibullin IH, Shulgin DA, Schmidt SV, Terukov EI (2012) Investigation of the promising thermoelectric compound $CuAlO_2$ by the method of nuclear quadrupole resonance in Cu. Semiconductors 46:1102–1105. https://doi.org/10.1134/S1063782612090163
5. Yamaguchi H, Ohtomo S, Kimura S, Hagiwara M, Kimura K, Kimura T, Okuda T, Kindo K (2010) Spiral-plane flop probed by ESR in the multiferroic triangular-lattice antiferromagnet $CuCrO_2$. Phys Rev B 81:033104. https://doi.org/10.1103/PhysRevB.81.033104
6. Kimura K, Nakamura H, Ohgushi K, Kimura T (2008) Magnetoelectric control of spin-chiral ferroelectric domains in a triangular lattice antiferromagnet. Phys Rev B 78:140401(R). https://doi.org/10.1103/PhysRevB.78.140401
7. Kimura K, Nakamura H, Kimura S, Hagiwara M, Kimura T (2009) Tuning ferroelectric polarization reversal by electric and magnetic fields in $CuCrO_2$. Phys Rev Lett 103:107201. https://doi.org/10.1103/PhysRevLett.103.107201
8. Soda M, Kimura K, Kimura T, Matsuura M, Hirota K (2009) Electric control of spin helicity in multiferroic triangular lattice antiferromagnet $CuCrO_2$ with proper-screw order. Jour Phys Soc Japan 78:124703. https://doi.org/10.1143/JPSJ.78.124703
9. Kimura K, Otani T, Nakamura H, Wakabayashi Y, Kimura T (2009) Lattice distortion coupled with magnetic ordering in a triangular lattice antiferromagnet $CuCrO_2$. Jour Phys Soc Japan 78:113710. https://doi.org/10.1143/JPSJ.78.113710
10. Koseoglu H, Turkoglu F, Kurt M, Yaman MD, Akca FG, Aygun G, Ozyuzer L (2015) Improvement of optical and electrical properties of ITO thin films by electroannealing. Vacuum 120:8–13. https://doi.org/10.1016/j.vacuum.2015.06.027
11. Zheng M, Ni J, Liang F, Wang MC, Zhao X (2016) Effect of annealing temperature on the crystalline structure, growth behavior and properties of SnO_2: Sb thin films prepared by radio frequency (RF)-magnetron sputtering. J Alloy Compd 663:371–378. https://doi.org/10.1016/j.jallcom.2015.12.037
12. Yan X, Li W, Aberle AG, Venkataraj S (2016) Investigation of the thickness effect on material and surface texturing properties of sputtered ZnO: Al films for thin-film Si solar cell applications. Vacuum 123:151–159. https://doi.org/10.1016/j.vacuum.2015.10.027
13. Thahab SM, Alkhayatt AH, Zgair IA (2016) Influences of post-annealing temperature on the structural and electrical properties of mixed oxides ($CuFeO_2$ and $CuFe_2O_4$) thin films prepared by spray pyrolysis technique. Mater Sci Semicond Process 41:436–440. https://doi.org/10.1016/j.mssp.2015.10.013
14. Shimode M, Sasaki M, Mukaida K (2000) Synthesis of the delafossite-type $CuInO_2$. J Solid State Chem 151:16–20. https://doi.org/10.1006/jssc.1999.8603
15. Krysa J, Keppert M, Jirkovsky JI, Stengl V, Subrt D (2004) The effect of thermal treatment on the properties of TiO_2 photocatalyst. J Mater Chem Phys 86:333. https://doi.org/10.1016/j.matchemphys.2004.03.021
16. Arda L (2019) The effects of Tb doped ZnO nanorod: An EPR study. Jour Mag and Mag Mat 475:493–501. https://doi.org/10.1016/j.jmmm.2018.11.121
17. Wang YD, Ma CL, Sun XD, Li HD (2002) Preparation and characterization of SnO_2 nanoparticles with a surfactant-mediated method. Nanotechnology 13:565. https://doi.org/10.1088/0957-4484/13/5/304
18. Tate J, Jayaraj MK, Draeseke AD, Ulbrich T, Sleight AW, Vanaja KA, Nagarajan R, Wager JF, Hoffman RL (2002) p-Type oxides for use in transparent diodes. Thin Solid Films 411:119. https://doi.org/10.1016/S0040-6090(02)00199-2
19. Wang Y, Gu Y, Wang T, Shi W (2011) Structural, optical and electrical properties of Mg-doped $CuCrO_2$ thin films by sol–gel processing. J Alloys Compd 509:5897–5902. https://doi.org/10.1016/j.jallcom.2011.02.175
20. Lin YJ, Luo J, Hung HC (2013) Electronic transport and Schottky barrier heights of p-type $CuAlO_2$ Schottky diodes. Appl Phys Lett 102(193511):12. https://doi.org/10.1063/1.4806970
21. Crottaz O, Kubel F (1996) Crystal structure of copper(I) chromium(III) oxide, 2H-$CuCrO_2$. Z Kristallogr 211(7):482–482. https://doi.org/10.1524/zkri.1996.211.7.481
22. Senol SD, Ozugurlu E, Arda L (2020) Synthesis, structure and optical properties of (Mn/Cu) co-doped ZnO nanoparticles. Jour of All and Comp 822:153514. https://doi.org/10.1016/j.jallcom.2019.153514
23. Senol SD, Ozugurlu E, Arda L (2020) The effect of cobalt and boron on the structural, microstructural, and optoelectronic properties of ZnO nanoparticles. Cer Int 46:7033–7044. https://doi.org/10.1016/j.ceramint.2019.11.193